Research Square

Preprints are preliminary reports that have not undergone peer review.
They should not be considered conclusive, used to inform clinical practice,
or referenced by the media as validated information.

The ranking of W-temper and warm forming of solution-treated AA7075 sheet reverses with strain path

Quang Hong Nguyen

t115569401@ntut.org.tw

National Taipei University of Technology

Imran Ismayil

National Taipei University of Technology

Liang-Yu Chen

National Taipei University of Technology

Hsuan Hsiao

National Taipei University of Technology

Yo-Lun Yang

National Taipei University of Technology https://orcid.org/0000-0001-5876-1644

Research Article

Keywords: AA7075, W temper, Warm forming, Forming limit, Nakajima test, Finite element simulation, Strain localisation

Posted Date: November 2nd, 2026

DOI: https://doi.org/10.21203/rs.3.rs-11359709/v1

License: This work is licensed under a Creative Commons Attribution 4.0 International License.
Read Full License

The ranking of W-temper and warm forming of solution-treated AA7075 sheet reverses with strain path

Hong-Quang Nguyen[1], Imran Ismayil[1], Liang-Yu Chen[1], Hsuan Hsiao[1] and Yo-Lun Yang[1,*]

[1]Graduate Institute of Manufacturing Technology, National Taipei University of Technology, Taipei 106, Taiwan

*Corresponding author: y.yang@ntut.edu.tw

Abstract

This study ranks W-temper and warm forming of solution-treated AA7075 sheet over seven strain paths rather than by one formability number. Nakajima blanks 16–100 mm wide were formed at 28 °C after quenching and at 100–180 °C after cooling from solution treatment. A finite element model and a plane-strain localisation analysis used the measured hardening laws and forming limit curves. The ranking of the routes reversed with strain path. On average, blanks 16–52 mm wide fractured 10.6–30.3% lower after warm forming than in the W temper, whereas blanks 86–100 mm wide fractured 5.7–30.1% higher. The width at which the routes swapped rank fell from 79.4 mm at 100 °C to 52.7 mm at 160 °C, with a tie over 50–74 mm at 180 °C. The model reproduced all 42 heights within 7.35% and the reversal. At 100–140 °C the plane-strain limit fell 41–58% below the limit that strain hardening allows, so deformation localised early. After paint bake, W-temper deformation gave up to 195.8 HV, against 172.6 HV for warm deformation. The strain path of the critical feature, rather than a single formability number, should therefore decide between W-temper and warm forming of solution-treated AA7075 sheet.

Keywords: AA7075; W temper; Warm forming; Forming limit; Nakajima test; Finite element simulation; Strain localisation

1. Introduction

AA7075 sheet has one of the highest specific strengths among wrought aluminium alloys, but in the peak-aged T6 temper its room-temperature formability is too low for most stamped parts [1, 2]. Two process routes avoid this limitation by forming the sheet from the solution-treated state [3, 4]. In W-temper forming, the sheet is quenched from the solution temperature and formed cold before natural ageing hardens it [5, 6]. In direct warm forming, the sheet is cooled to the forming temperature and formed there, and the same temperature then serves as the first ageing step [7, 8]. Both routes end in artificial ageing, which in automotive production can be combined with the paint-bake cycle [6, 8]. The choice between the routes for a given part turns on three questions. The first is whether strain path changes the ranking of the two routes. The second concerns the mechanism that limits the forming strain of each route. The third concerns the hardness that each route leaves after the paint bake.

Forming in the W temper exploits the low flow stress and the high ductility of the freshly quenched solid solution [5, 9]. Choi et al. [5] measured a plane-strain forming limit of 0.154

for W-temper 7075 sheet, against 0.091 in the T6 temper. Lee et al. [6] formed automotive parts from W-temper sheet and restored their strength by ageing combined with paint baking. The quenched alloy, however, hardens by natural ageing within hours, and its properties depend on the quench rate [7, 9]. W-temper 7075 also flows in a serrated manner, and Portevin–Le Chatelier (PLC) bands have been observed in it during hole expansion [10].

Warm forming instead lowers the flow stress by heating [11, 12]. Applied to T6 sheet, it raises the ductility of AA7075 but risks over-ageing, so the heating time must be kept short [13–15]. Applied to solution-treated sheet, warm forming couples deformation with the first ageing step, as in the ageing warm-forming process of Chen and Lee [16]. Zheng et al. [8] also compared several elevated-temperature routes and found that the post-formed strength depends on the sequence of forming and ageing. Finite element (FE) models of AA7075 at elevated temperature have combined calibrated flow curves with forming limit curves or damage criteria to predict forming limits [17–19]. Our previous study [7] reported the tensile behaviour, the forming limit curves (FLCs) and the ageing response of solution-treated AA7075 at room temperature and at 100–180 °C. From tensile data, that study placed a forming window near 160 °C, but it did not compare the fracture heights of the two routes across blank widths.

Comparisons of tempers and forming temperatures for AA7075 have rested on single numbers, such as the tensile elongation, the limiting dome height (LDH) or the plane-strain forming limit (FLD_0) [5, 7, 11]. Each such number ranks the conditions for one strain path, and the ranking is then assumed to hold for every other path. Formability theory, however, gives reasons to doubt this assumption. The analyses of Hill [20], of Marciniak and Kuczyński [21] and of Hutchinson and Neale [22] tie the forming limit to the strain hardening of the sheet. Strain-rate sensitivity shifts the limit further, upwards when it is positive and downwards when it is negative [23–25]. Strain hardening and rate sensitivity both change between a cold and a warm solid solution, because solute atoms age dynamically and cluster during straining [26–28]. Temperature and strain rate are known to change the shape, and not only the level, of the forming limit curves of other aluminium alloys [29, 30]. The two routes may therefore rank differently on the drawing side and on the stretching side of the forming limit diagram (FLD) [31, 32].

Nakajima tests on blanks of seven widths give the fracture height of each route over strain paths from the drawing side of the FLD to biaxial stretching. In these tests the W temper is

formed at 28 °C, and the warm route at 100, 120, 140, 160 and 180 °C after cooling from solution treatment. An FE model built on the measured hardening laws and FLCs then tests whether these two inputs account for the ranking. A plane-strain localisation analysis compares each measured forming limit with the limit that strain hardening alone allows. Hardness after a two-stage ageing that ends in a paint bake measures the strength each route leaves. The present work thus compares the two routes on the strain path of the part rather than on a single formability number.

2. Materials and methods

2.1. Material and processing routes

Both routes were applied to commercial AA7075-T6 sheet, 2 mm thick. The as-received sheet had a tensile strength of 509.2 MPa, a 0.2% proof stress of 418.8 MPa and an elongation of 11.9% [7]. The Vickers hardness of the T6 sheet was 162 HV. Both routes started with solution heat treatment (SHT) at 477 °C for 15 min, a holding time that dissolved the strengthening precipitates as fully as 60 and 120 min did [7].

In Route 1, the sheet was quenched in water after SHT and formed immediately at 28 °C in the W temper (Fig. 1a). The formed sheet is then aged at 100, 120, 140, 160 or 180 °C for 120 min and paint baked at 185 °C for 20 min. In Route 2, the sheet was cooled at about 55 °C s^{-1} to 100, 120, 140, 160 or 180 °C and formed at that temperature (Fig. 1b). The formed sheet is then held at the forming temperature for 120 min as the first ageing stage and paint baked in the same way. In Route 2 the first ageing temperature therefore equals the forming temperature, whereas Route 1 sets the two independently (Table 1).

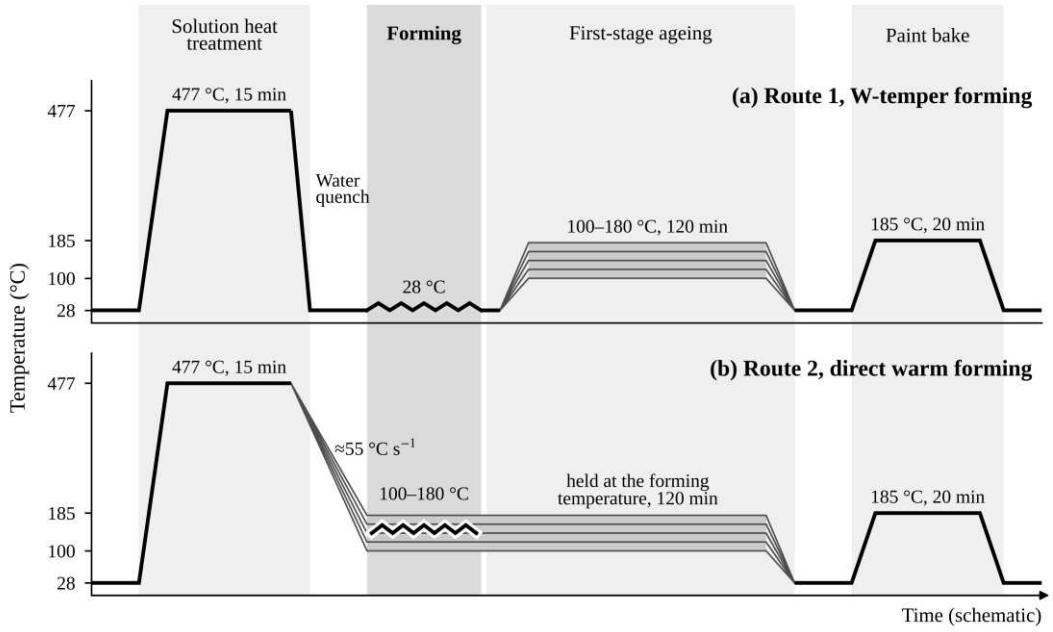


Fig. 1. Thermal schedules of (a) Route 1, W-temper forming, and (b) Route 2, direct warm forming. The temperature axis is to scale and the time axis is schematic.

2.2. Experimental design

The test matrix sets up three contrasts. Route is varied at a fixed blank width by comparing each warm temperature with the W temper. Strain path is varied within each route by seven blank widths, from the drawing side of the FLD in the narrowest blank to biaxial stretching in the full blank. Ageing is varied for both routes over 100–180 °C, with undeformed material aged in the same two stages as a baseline [7].

2.3. Nakajima tests and forming limit curves

Stretch formability was measured by Nakajima tests scaled down from ISO 12004-2 [33] on a sheet-metal forming tester (Amino, Japan) with heated tooling. A hemispherical punch of 50 mm diameter stretched the blank through a 54 mm opening with a 5 mm profile radius (Fig. 2a). The blank was clamped with a force of 140 kN, and the punch advanced at 1.5 mm min^{-1}. Stamping oil and a thin polyethylene film lubricated the punch contact. All blanks were 100 mm in diameter, the full disc and six blanks with a neck of width w = 86, 72, 52, 40, 28 and 16 mm (Figs. 2b and 3). In Route 2, the blanks were cooled from the SHT temperature to the forming temperature and tested in tooling held at that temperature.

Each test was stopped when a crack became visible, and the punch travel at that moment was recorded as the fracture height H_{EXP}. A circle grid, laser-engraved on each blank before forming, was measured near the crack by circle grid analysis [34, 35]. Each circle was

classified as safe, necked or fractured [7] (Fig. 4a–f). The FLC at each temperature was fitted to the boundary between the safe and the fractured circles with a shifted parabola [7],

$$\varepsilon_1 = a + k\,(\varepsilon_2 - p)^2. \tag{1}$$

Here ε_1 and ε_2 are the major and minor strains, a is the vertex value, p the vertex position on the minor-strain axis and k the curvature coefficient. The plane-strain limit follows as $FLD_0 = a + kp^2$. The measured circles span minor strains from −0.08 to 0.10, and the narrowest span, at 28 °C, runs from −0.02 to 0.08 (Table 2). Each FLC is extrapolated outside these spans, as the dotted lines of Fig. 4g show.

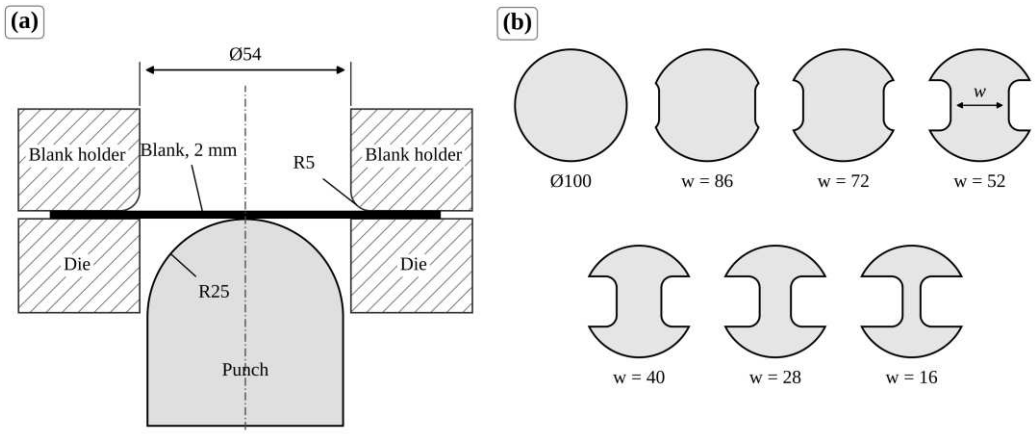


Fig. 2. Nakajima tooling in section (a) and the seven blanks of width w (b), both drawn to scale. The notched blanks have 45 mm side slots with 10 mm fillets.

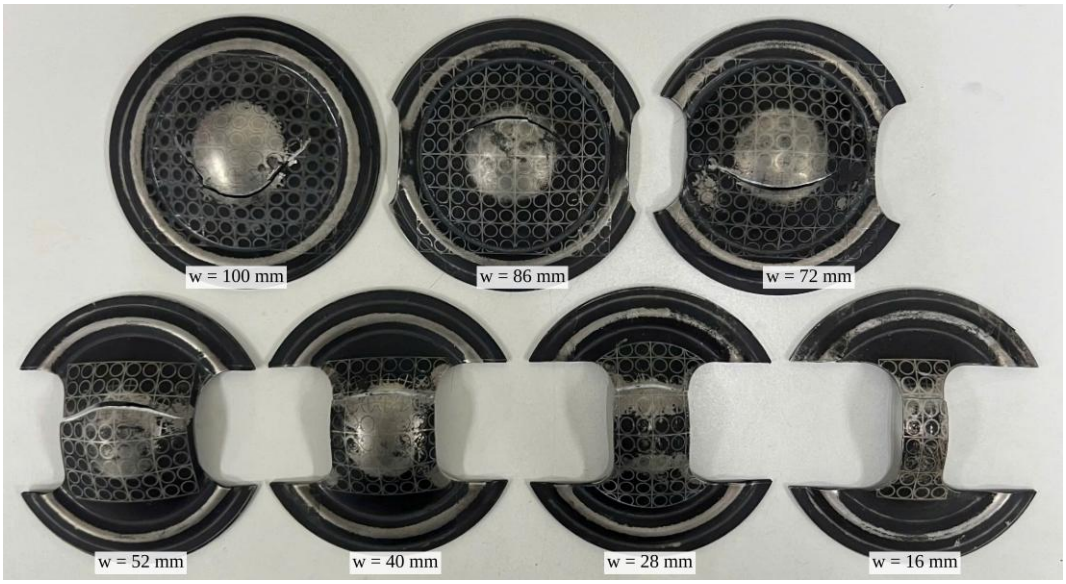


Fig. 3. The seven blanks after testing, with the laser-engraved circle grid and the crack of each blank visible.

Table 2. Forming limit curves of Eq. (1) fitted to the circle-grid data of [7], with the span of minor strain covered by the measured circles.

T (°C)	a	k	p	R^2	RMSE	Measured ε_2
28	0.1297	12.9954	0.0395	0.553	0.0091	−0.02 to 0.08
100	0.0981	4.2564	0.0066	0.591	0.0066	−0.08 to 0.10
120	0.1086	13.1057	0.0342	0.643	0.0163	−0.04 to 0.10
140	0.1183	13.8031	0.0253	0.611	0.0185	−0.05 to 0.10
160	0.1367	1.5245	0.0909	0.579	0.0071	−0.05 to 0.10
180	0.2116	−0.2962	−0.1763	0.402	0.0061	−0.04 to 0.09

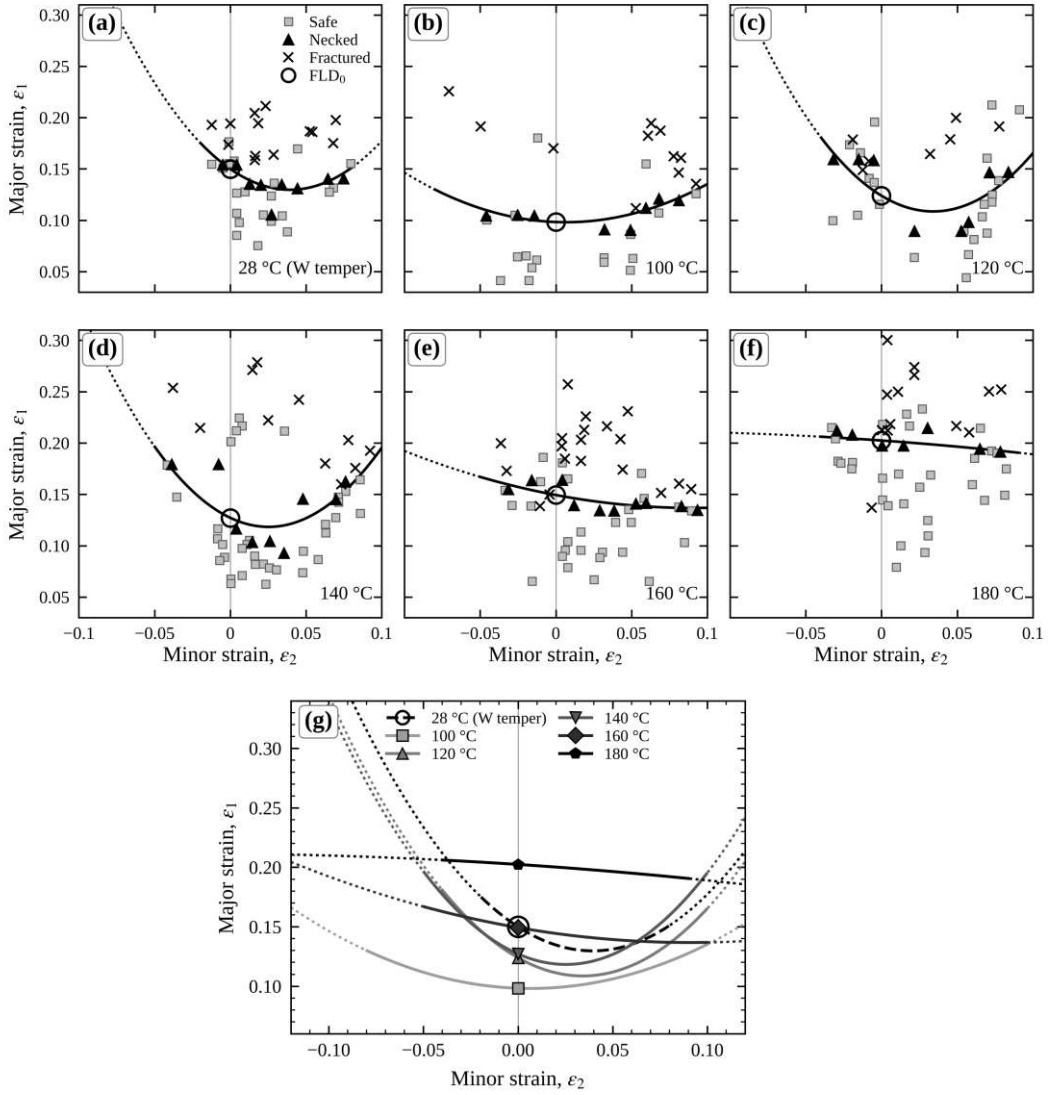


Fig. 4. Forming limit diagrams at the six forming temperatures (a–f), with the circles classified as safe, necked or fractured and the fitted FLC, and (g) the six FLCs used as FE input. Solid curves cover the minor strains of the measured circles, dotted curves are extrapolations, and the open circles give FLD_0.

2.4. Tensile tests and hardening law

The hardening laws, the second input of the FE model, came from uniaxial tensile tests. Room-temperature tests were run on a universal testing machine (YM-H5103-A01, Yangyi

Technology, 100 kN) with an extensometer of 25 mm gauge length (Epsilon 3542). Warm tests were run on a Gleeble-3500 simulator, which heated the specimen by direct resistance in argon and controlled its temperature through a spot-welded K-type thermocouple. The flow curves, tensile strengths and elongations at 0.1, 0.5 and 1.0 s^{-1} were reported previously [7]. A W-temper specimen cut at 90° to the rolling direction followed the hardening law calibrated at 0° to within 2% above a plastic strain of 0.08 (Fig. 5a). The sheet was therefore treated as isotropic.

The FE model needs flow stresses beyond uniform elongation, where the Swift law hardens without bound and the Voce law saturates too early [36]. The linear Swift–Voce (LSV) law interpolates between these two extrapolations [36–38],

$$\bar{\sigma} = \alpha C (\varepsilon_0 + \bar{\varepsilon})^n + (1 - \alpha)\left[A - B \exp(-\beta \bar{\varepsilon})\right]. \tag{2}$$

Here $\overline{\sigma}$ is the flow stress and $\overline{\varepsilon}$ the equivalent plastic strain. The Swift parameters are C, ε_0 and n, the Voce parameters A, B and β, and α weights the Swift term. The parameters were fitted by least squares to the true stress–strain curve at each temperature (Table 3, Fig. 5b). The von Mises yield criterion was used.

Table 3. Parameters of the LSV law, Eq. (2).

T (°C)	C (MPa)	ε_0	n	A (MPa)	B (MPa)	β	α
28	746.45	0.011	0.318	468.90	282.91	11.06	0.275
100	700.69	0.027	0.385	441.19	263.95	7.60	0.350
120	643.80	0.020	0.342	407.00	233.39	9.18	0.348
140	642.93	0.022	0.337	409.85	228.26	9.06	0.622
160	623.71	0.024	0.338	407.99	227.87	8.38	0.530
180	563.06	0.018	0.293	380.79	203.15	9.59	0.573

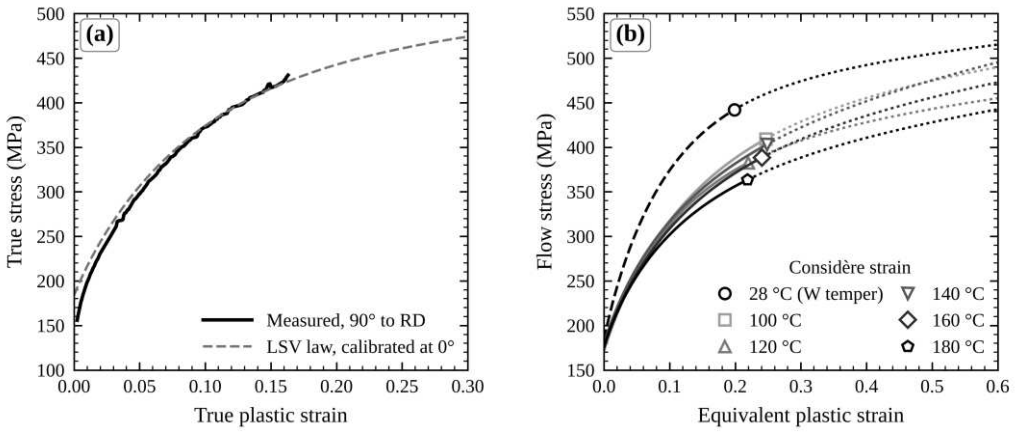


Fig. 5. (a) The W-temper flow curve measured at 90° to the rolling direction follows the LSV law calibrated at 0°. (b) The LSV laws of all six temperatures, dashed for the W temper, are drawn up to their Considère strain (open markers) and dotted beyond.

2.5. Hardness

Vickers hardness was measured after the paint bake on tensile specimens that followed the thermal history of each route. Route 1 specimens were quenched, pre-strained by about 20% at 0.1 s^{-1} in the W temper and aged, with 3 days at room temperature between the two ageing stages [7]. Route 2 specimens were deformed in tension at the forming temperature, held there for 120 min and paint baked. Undeformed material, cooled from the SHT temperature directly to the first-stage ageing temperature and aged in the same two stages, served as the baseline [7].

3. Modelling

3.1. FE model of the Nakajima test

The Nakajima test was modelled in Abaqus/Explicit with the tool geometry of Fig. 2a. The punch, die and blank holder were rigid, and the blank was meshed with S4R shell elements of about 0.5 mm. Contact followed Coulomb friction with a coefficient of 0.1, and the blank holder applied 140 kN as in the tests. The punch moved at 1.5 mm s^{-1}, which shortens the explicit analysis and leaves the rate-independent material response unchanged. Each run used the LSV law and the FLC of its forming temperature, and nothing else differed between the runs. Since the FLCs were measured on the tested blanks themselves, the runs test whether these two inputs account for the measured heights and their ranking.

Failure was predicted with the FLD damage-initiation criterion of Abaqus [39]. At every integration point, the criterion compares the current major strain with the FLC value at the current minor strain, $\omega = \varepsilon_1/\varepsilon_1^{\mathrm{FLC}}(\varepsilon_2)$. The predicted fracture height H_{FE} is the punch travel at which ω first reaches 1 in any element, and the prediction error is

$$E_H = \frac{H_{\mathrm{EXP}} - H_{\mathrm{FE}}}{H_{\mathrm{EXP}}} \times 100\%. \tag{3}$$

The error is positive when the model is conservative.

3.2. Plane-strain localisation analysis

The plane-strain point of each FLC can be compared with the limit that strain hardening alone would allow [20]. In plane strain with von Mises plasticity, the load per unit width $\sigma_1 t$ reaches its maximum when

$$\frac{1}{\bar{\sigma}}\frac{\mathrm{d}\bar{\sigma}}{\mathrm{d}\bar{\varepsilon}} = \frac{\sqrt{3}}{2}, \tag{4}$$

and the major strain at that instant, $\varepsilon_1^* = (\sqrt{3}/2)\,\bar{\varepsilon}^*$, is the Hill limit [20]. For a power-law material, ε_1^* equals the hardening exponent, as in the Considère condition for uniaxial tension. For the LSV law, Eq. (4) was solved numerically at each temperature, and ε_1^* then equals the effective hardening exponent $n_{\mathrm{eff}} = (\bar{\varepsilon}/\bar{\sigma})\,\mathrm{d}\bar{\sigma}/\mathrm{d}\bar{\varepsilon}$ at $\bar{\varepsilon}^*$.

The localisation index

$$\lambda = 1 - \mathrm{FLD}_0/\varepsilon_1^* \tag{5}$$

measures the fraction of the hardening-controlled limit that a sheet loses to early localisation. The same comparison can be expressed through the imperfection model of Marciniak and Kuczyński [21], by considering a groove whose initial thickness is f_0 times that of the surrounding sheet. Force equilibrium across the groove in plane strain gives

$$\bar{\sigma}\left(\tfrac{2}{\sqrt{3}}\varepsilon_1^a\right) e^{-\varepsilon_1^a} = f_0\,\bar{\sigma}\left(\tfrac{2}{\sqrt{3}}\varepsilon_1^b\right) e^{-\varepsilon_1^b}, \tag{6}$$

where the superscripts a and b denote the sheet and the groove. The load per unit width in the groove peaks when ε_1^b reaches ε_1^*, so the imperfection that reproduces a measured plane-strain limit is

$$f_0 = \frac{\bar{\sigma}\left(2\,\mathrm{FLD}_0/\sqrt{3}\right) e^{-\mathrm{FLD}_0}}{\bar{\sigma}\left(2\,\varepsilon_1^*/\sqrt{3}\right) e^{-\varepsilon_1^*}}. \tag{7}$$

This rate-independent estimate needs only the LSV law and FLD_0. The strain-rate sensitivity, which Eq. (7) leaves out, was derived from the tensile strengths at 0.1 and 1.0 s^{-1} [7] as

$$m = \frac{\ln\left(\sigma_{\mathrm{UTS}}^{1.0}/\sigma_{\mathrm{UTS}}^{0.1}\right)}{\ln 10}. \tag{8}$$

4. Results

4.1. Route ranking by blank width

On average, the two routes respond to blank width in opposite directions (Fig. 6). In the W temper, the narrow blanks (w = 16–52 mm) fractured 3.2 mm higher on average than the wide blanks (w = 86–100 mm). The 72 mm blank, near which the ranking changes, belongs to

neither group. Under warm forming, the order of the two groups was reversed at every temperature, with the wide blanks higher by 0.5–3.4 mm. The full blank alone would therefore rank warm forming first at every temperature, its height rising from 15.38 mm in the W temper to 19.87 mm at 180 °C.

On the narrow blanks the ranking is the opposite (Fig. 7a). Every narrow blank fractured lower after warm forming than in the W temper, by 0.10–6.64 mm. The mean height of these four blanks lay 30.3% below the W temper at 100 °C and 10.6–12.7% below it at 120–180 °C. Forming at 100 °C gave the lowest height of all conditions, 12.35–15.64 mm, for every blank of 16–72 mm. On the wide blanks, every warm-formed blank fractured higher, by 0.60–4.86 mm. The mean height of these blanks rose from 5.7% above the W temper at 100 °C to 30.1% at 180 °C.

From 100 to 160 °C, the width at which the two routes give equal heights moves to narrower blanks (Fig. 7c). This crossover width falls from 79.4 mm at 100 °C through 76.6 mm and 69.4 mm to 52.7 mm at 160 °C. Differences smaller than 0.5 mm are treated as ties. This threshold is twice the standard deviation of a height difference, estimated from the 0.18 mm scatter of the measured heights about the FE prediction. Of the 35 route differences, 30 exceed this threshold. At 180 °C the sign changes at 73.0 mm, but the two routes stay within 0.5 mm of each other from 50 to 74 mm.

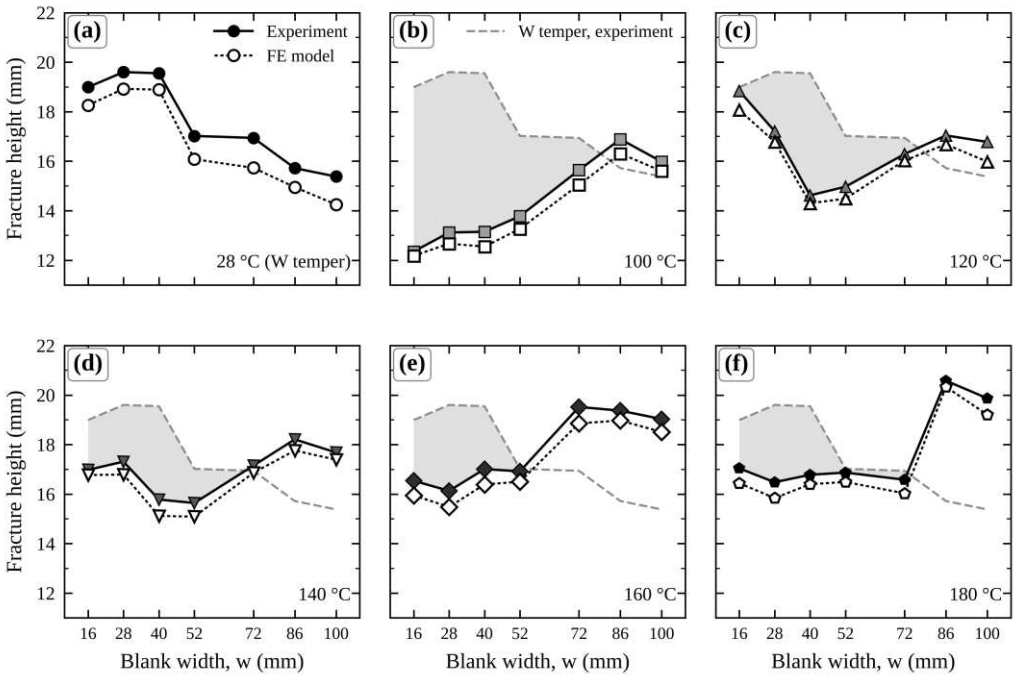


Fig. 6. Fracture height against blank width at each forming temperature, measured (filled) and predicted by the FE model (open). In the warm panels the dashed line repeats the W-temper measurement, and shading marks the widths at which the warm-formed blank fractured lower.

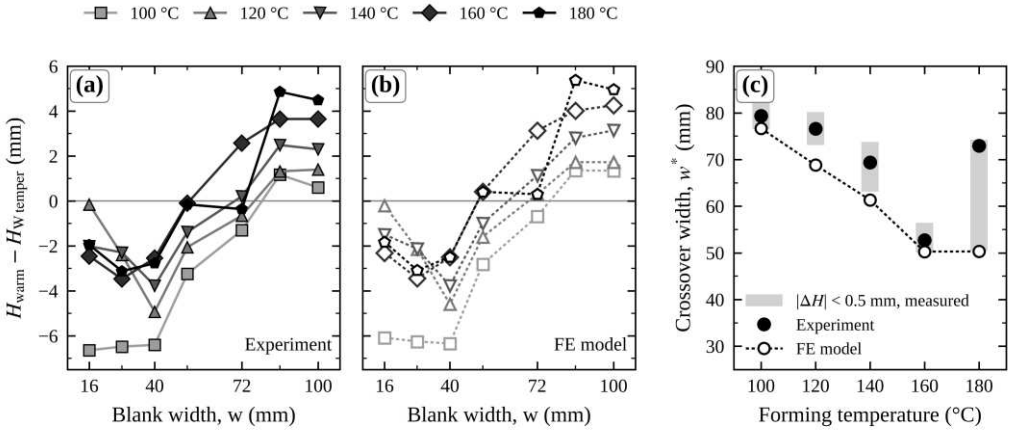


Fig. 7. Height difference between warm forming and the W temper against blank width, (a) measured and (b) predicted, and (c) the crossover width at which the difference changes sign. Grey bars in (c) span the widths over which the measured difference stays within 0.5 mm of zero.

4.2. FE model against the measured heights

With the hardening law and the FLC as its only temperature-dependent inputs, the FE model predicted all 42 fracture heights (Fig. 8a). The prediction error was smaller under warm forming, 1.21–4.77% with a mean of 2.9%, than in the W temper, 3.38–7.35% with a mean of 5.1% (Table A.1). Over all tests, the predicted and measured heights differed by 0.59 mm in root-mean-square terms, with a correlation coefficient of 0.993.

Every prediction fell below its measurement, so the deviation is mainly a conservative offset (Fig. 8b). The offset averaged 0.49 mm under warm forming and 0.87 mm in the W temper. The FE height marks the first element that reaches the FLC anywhere in the blank, whereas each test was stopped when a crack became visible. A positive offset is therefore expected.

The model also reproduces the reversal of the route ranking (Fig. 7b). The predicted height difference between the routes has the measured sign in 31 of the 35 width–temperature pairs. The four exceptions lie at 52 and 72 mm, where the measured difference is 0.65 mm or less. The predicted crossover width falls from 76.7 mm at 100 °C to 50.3 mm at 160 °C and stays there at 180 °C. These predicted crossovers lie at narrower blanks than the measured ones, because the larger W-temper offset raises every predicted route difference by about 0.4 mm. With the mean offset of each temperature removed, 33 of the 35 differences take the measured sign, and every predicted crossover lies within 4 mm of the measured one.

At 140 °C the model predicts the crack across the neck of the 16 mm blank and around the dome of the full blank, as observed (Fig. 9a,c). In the 52 mm blank, however, the predicted crack lies nearer the pole than the observed one (Fig. 9b). On the full blank, the predicted height rises with forming temperature, as the measured one does (Fig. 9d–g).

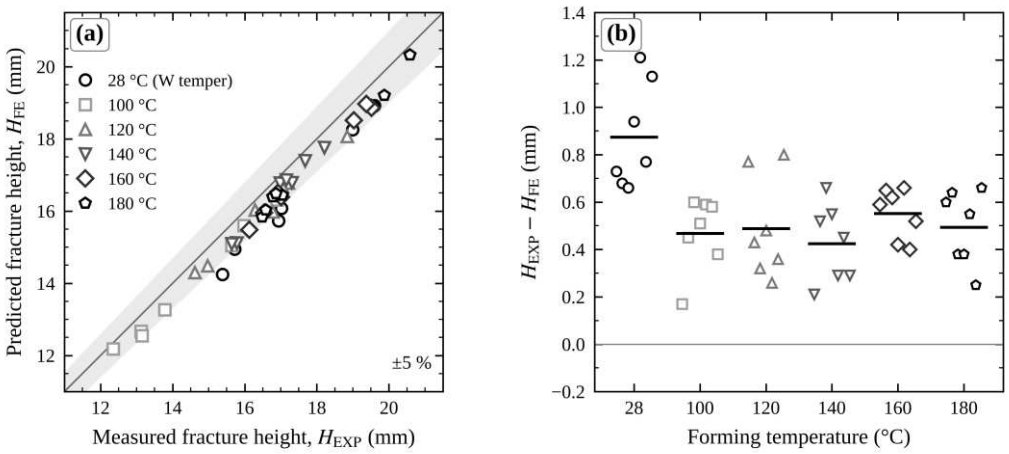


Fig. 8. (a) Predicted against measured fracture height for all 42 tests, with the ±5% band shaded. (b) Offset between measured and predicted height, with the points of each temperature ordered by blank width and the mean marked by a bar.

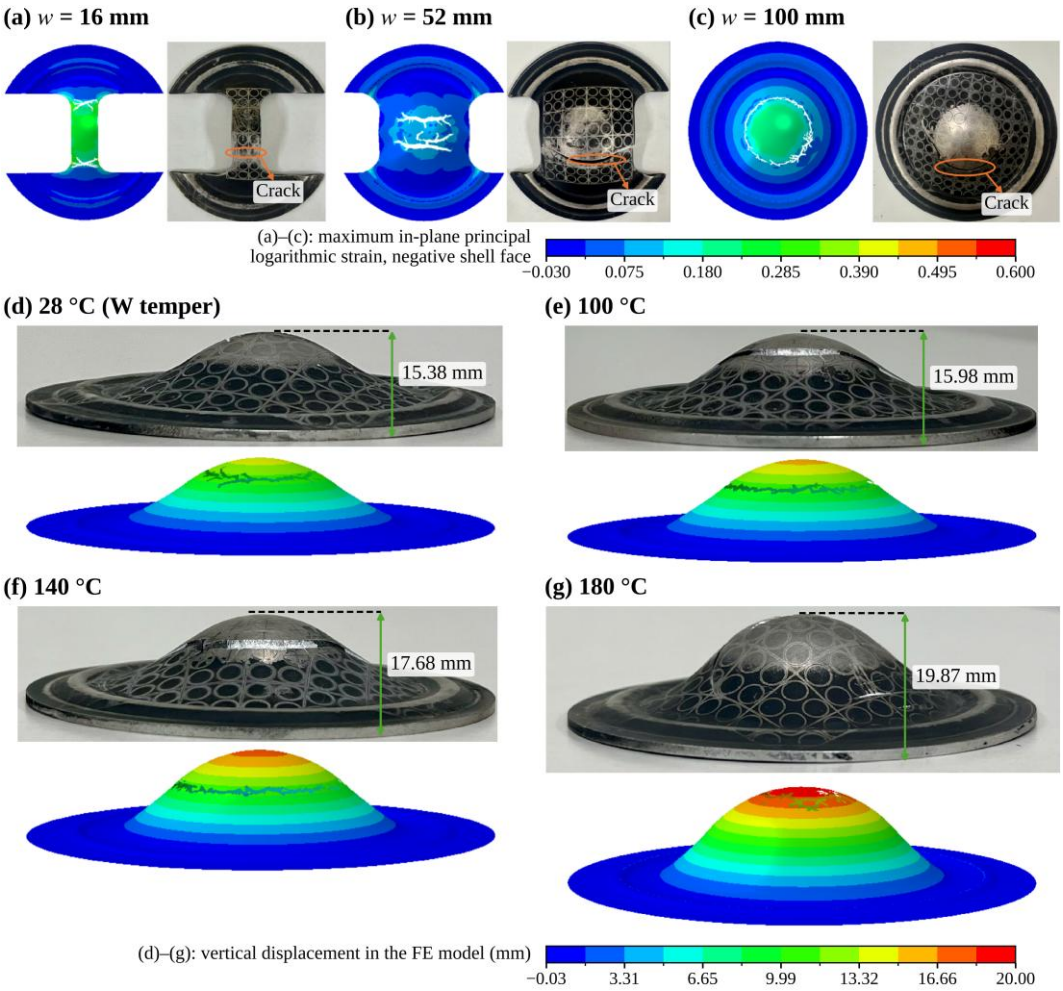


Fig. 9. (a)–(c) Predicted maximum in-plane principal logarithmic strain beside the tested blank at 140 °C for widths of 16, 52 and 100 mm, with the observed cracks ringed. (d)–(g) Full blanks formed in the W temper and at 100, 140 and 180 °C, with the measured fracture height, above the FE prediction coloured by vertical displacement. All side views share one scale, and white (a)–(c) and dark (d)–(g) bands in the FE fields are the predicted cracks.

4.3. Plane-strain limit against the hardening limit

Of the two FE inputs, FLD_0 changes far more with temperature than the Hill limit of the hardening law (Fig. 10b). FLD_0 falls from 0.150 in the W temper to 0.098 at 100 °C and then rises to 0.202 at 180 °C (Table 4). The Hill limit of the six LSV laws, in contrast, stays between 0.187 and 0.243. Every law reaches its plane-strain load maximum at $\overline{\varepsilon}$ of 0.22–0.28, after n_{eff} has passed its peak (Fig. 10a).

The shortfall of FLD_0 below the Hill limit is largest at 100–140 °C. The localisation index is 0.41–0.58 at 100–140 °C and 0.36 at 160 °C, against 0.20 in the W temper and 0.05 at 180 °C. Replacing ε_1^* by the uniaxial Considère strain changes λ by 0.04 at most and keeps this grouping. In the imperfection model, a groove 0.8% thinner than the sheet reproduces

FLD_0 in the W temper, 2.6% at 160 °C and under 0.1% at 180 °C. At 100–140 °C, however, the groove would have to be 3.8–9.8% thinner.

The tensile elongation at fracture falls where the localisation index rises (Fig. 10c). The elongation is lowest at 100 °C, 21.7%, and highest at 180 °C, 27.6% [7]. The correlation coefficient between the elongation and the localisation index is −0.94, with or without the W temper. The strain-rate sensitivity from the same tensile tests is negative at every temperature, most negative at 100 °C (−0.025) and least negative at 180 °C (−0.011).

Table 4. Plane-strain localisation analysis, with the effective hardening exponent at $\bar{\varepsilon} = 0.02$. Elongation is at fracture in tension at 0.1 s^{-1} [7].

T (°C)	FLD_0	ε_1^*	λ	$1 - f_0$ (%)	n_{eff} at 0.02	m	Elongation (%)
28	0.150	0.187	0.20	0.8	0.207	−0.017	26.0
100	0.098	0.236	0.58	9.8	0.162	−0.025	21.7
120	0.124	0.209	0.41	3.8	0.169	−0.017	22.0
140	0.127	0.243	0.48	4.9	0.159	−0.017	23.0
160	0.149	0.233	0.36	2.6	0.152	−0.016	24.8
180	0.202	0.212	0.05	<0.1	0.153	−0.011	27.6

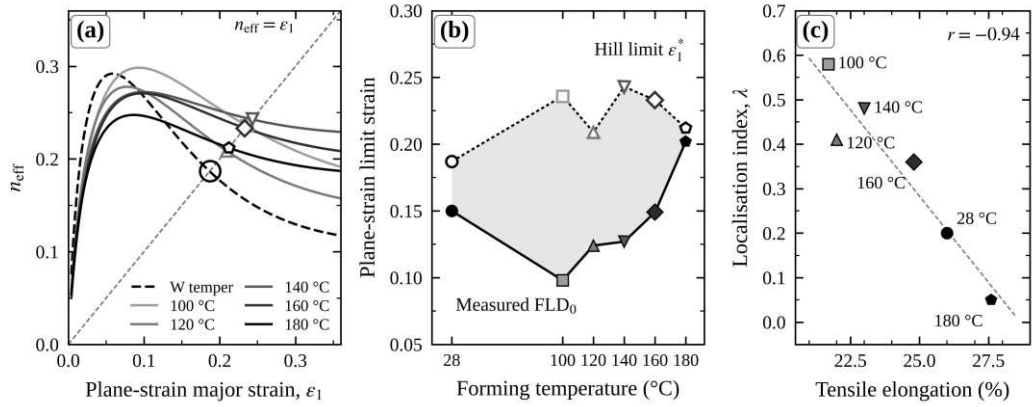


Fig. 10. (a) Effective hardening exponent of each LSV law against the plane-strain major strain, whose intersection with the diagonal gives the Hill limit (open markers). (b) Measured FLD_0 (filled) and Hill limit (open) against forming temperature, and (c) localisation index against the tensile elongation of [7].

4.4. Hardness after paint bake

Route 1 left a higher hardness after paint bake than Route 2 at every ageing temperature (Fig. 11). Route 1 peaked at 195.8 HV after first-stage ageing at 120 °C, 20.9% above the T6 value, and fell to 155.3 HV at 180 °C [7]. Route 2 reached 163.4, 158.0, 172.6, 159.5 and 135.5 HV at 100, 120, 140, 160 and 180 °C. The Route 2 peak, at 140 °C, lies 6.5% above T6 but 11.8% below the Route 1 peak.

Relative to the undeformed baseline, Route 1 added 15.6–34.8 HV, whereas Route 2 added −4.3 to +16.7 HV. From 100 to 160 °C, Route 2 kept the hardness within −2.5% to +6.5% of T6, while at 180 °C the hardness fell 16.4% below T6.

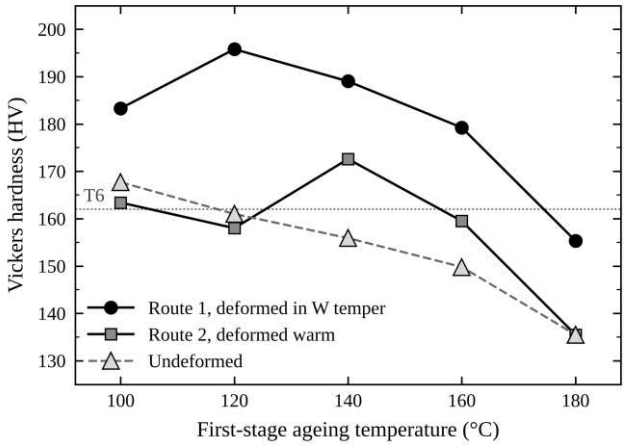


Fig. 11. Vickers hardness after paint bake against first-stage ageing temperature, with the T6 value dotted. Route 1 and undeformed data are from [7], and in Route 2 the ageing temperature equals the forming temperature.

5. Discussion

The Introduction asked whether strain path changes the ranking of the two routes and which mechanism limits the forming strain of each route. The third question concerned the hardness each route leaves after paint bake.

5.1. Strain path and the ranking of the routes

Within Route 2, the plane-strain limit ranks the mean fracture heights at both ends of the width range. From 100 to 180 °C, FLD_0 rises monotonically, and the mean heights of the narrow and of the wide blanks rise in the same order. Warm forming at a higher temperature therefore raises the mean height of both groups, because the sheet localises later.

The W temper does not follow the order set by the plane-strain limit. The W-temper plane-strain limit equals that at 160 °C. Yet the W temper forms the narrow blanks 2.1 mm higher and the wide blanks 3.7 mm lower than warm forming at 160 °C. The route effect therefore lies away from plane strain, in aspects of the material response that FLD_0 does not measure. The W temper hardens fastest of all conditions at small strain (Table 4) but slowest beyond a plane-strain major strain of about 0.2 (Fig. 10a). Fast early hardening spreads strain over the punch [23], whereas weak hardening at large strain lets the strain concentrate. Biaxial

stretching reaches the largest equivalent strains, so the wide blanks suffer most from the weak late hardening of the W temper. On the drawing side, the W-temper FLC also rises steeply, whereas the 160 °C curve is nearly flat (k = 13.0 against 1.5). The narrow blanks, which strain towards negative minor strain, therefore favour the W temper.

On the wide blanks, the FE model reproduces the W-temper deficit, with a predicted full-blank height of 14.25 mm against 18.51 mm at 160 °C. Since the 28 °C and 160 °C runs differ only in the hardening law and the FLC, the deficit comes from these two inputs. A route that stretches well biaxially therefore does not necessarily form well on the drawing side, and the full-blank height alone cannot show the difference. The crossover width shows the difference instead, as one number for each forming temperature, and from 100 to 160 °C it falls as FLD_0 recovers. At 180 °C the routes tie on the 52 and 72 mm blanks, although FLD_0 is highest there. The 180 °C law, however, hardens least of all at strains of 0.05 and 0.10, with n_{eff} of 0.224 and 0.248. The FE model reproduces the tie once its offset is removed. This ranking qualifies the earlier conclusion, drawn from the same FLDs, that warm forming widens the safe region along every strain path [7].

5.2. Localisation at 100–140 °C

Strain hardening cannot explain the low plane-strain limit at 100–140 °C, because the Hill limit there is as high as at any other temperature. The sheet therefore localises before the hardening-controlled limit, through a mechanism that the rate-independent LSV law does not contain. The groove of 3.8–9.8% needed at 100–140 °C is five to thirteen times the 0.8% that reproduces the W-temper limit of the same sheet. Since the sheet and its thickness variation are the same at every temperature, the extra localisation must arise during deformation at 100–140 °C. The groove shrinks to 2.6% at 160 °C and below 0.1% at 180 °C, so the extra localisation fades above 140 °C rather than stopping abruptly. The tensile elongation, lowest at 100–140 °C, shows that this localisation also develops within the few seconds of a tensile test.

Two processes in the supersaturated matrix are proposed as its causes. The first is dynamic strain ageing, which makes the rate sensitivity most negative at 100 °C and so concentrates strain into bands [26, 27, 40]. The low and heterogeneous dislocation density observed after deformation at 100 °C [7] is consistent with such banding. At 120 and 140 °C, however, the rate sensitivity equals that of the W temper, so dynamic strain ageing alone cannot explain the low limit there. The second process is solute clustering, which starts within seconds of

quenching in supersaturated Al–Zn–Mg–Cu alloys [28, 41]. At 120–140 °C the clusters form during the test itself, whereas natural ageing at 28 °C takes hours [7]. Shearable solute clusters favour coarse planar slip, so strain concentrates in slip bands [42]. Above 140 °C, faster recovery by cross-slip and climb is expected to spread the strain more evenly, as the dense dislocation tangles after deformation at 180 °C suggest [7].

For process design, the 100–140 °C window is the least attractive part of Route 2. Forming at 100 °C, for example, combines the lowest heights on the blanks up to 72 mm with no hardness gain over undeformed material. Above 140 °C the plane-strain limit recovers, and at 160 °C so does the reach of warm forming towards narrower blanks.

5.3. Hardness and the choice of route

Route 1 lifts the aged hardness well above that of undeformed material, in line with the dislocation-assisted precipitation reported for pre-strained material [7, 43]. Warm deformation adds far less hardness, so the final hardness of Route 2 is set mainly by the forming temperature, which doubles as the ageing temperature. Above 160 °C both routes over-age, as the coarse precipitates and extensive grain-boundary precipitation observed after ageing at 180 °C indicate [7].

The route should be chosen by the strain path of the critical feature of the part, with the required strength as the second criterion (Fig. 12). For features that strain on the drawing side, represented by the narrow blanks, the W temper is better on both counts. Route 1 forms these blanks higher than any warm temperature and, aged at 120 °C, reaches the highest hardness of all conditions. For biaxially stretched features, represented by the wide blanks, warm forming is better, but its hardness falls above 140 °C. Warm forming at 160 °C raises the mean height of the wide blanks by 23.5% over the W temper and keeps the hardness at the T6 level. Warm forming at 140 °C gives a smaller gain, 15.4%, but the highest Route 2 hardness. Forming at 180 °C forms the wide blanks highest of all but leaves the hardness well below T6, which rules it out for structural parts.

A single formability number would have hidden the choice between the routes. The full-blank height alone, for example, favours warm forming at every temperature, and FLD_0 alone favours 180 °C, yet no route or temperature is best for every feature. The strain path of the critical feature should therefore decide between the two routes.

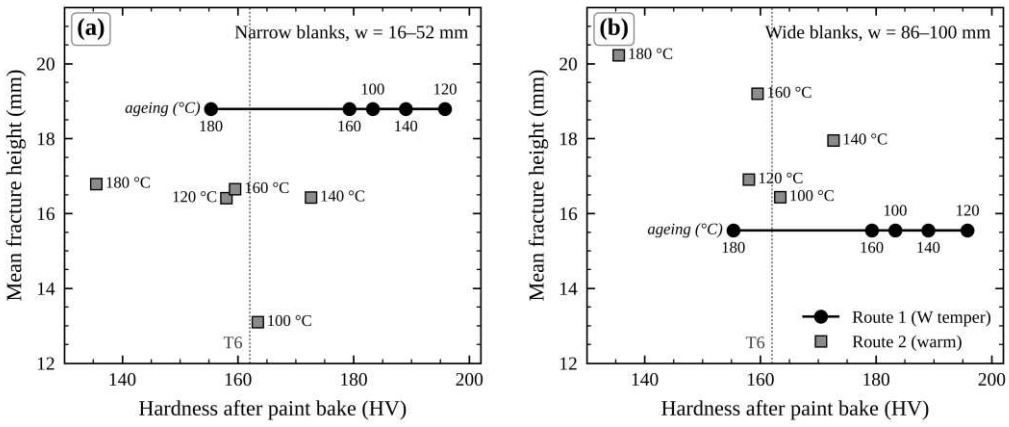


Fig. 12. Mean fracture height against hardness after paint bake for (a) the narrow blanks (w = 16–52 mm) and (b) the wide blanks (w = 86–100 mm). Route 1 points are labelled with the first-stage ageing temperature and Route 2 points with the forming temperature.

6. Conclusions

This study compared W-temper forming at 28 °C with direct warm forming at 100–180 °C of solution-treated AA7075 sheet on Nakajima blanks of seven widths. The comparison also used an FE model, a plane-strain localisation analysis and hardness after paint bake.

1. The ranking of the two routes reverses with strain path. On average, blanks of 16–52 mm fractured 10.6–30.3% lower after warm forming than in the W temper, whereas blanks of 86–100 mm fractured 5.7–30.1% higher. The width at which the routes swap rank fell from 79.4 mm at 100 °C to 52.7 mm at 160 °C, with a tie over 50–74 mm at 180 °C. With the hardening law and the FLC as its only temperature-dependent inputs, an FE model reproduced all 42 heights within 7.35% and also the reversal.

2. The plane-strain limit varied twofold with temperature, from 0.098 to 0.202, while the limit allowed by strain hardening stayed between 0.187 and 0.243. Localisation is therefore strongest at 100–140 °C, where a thickness imperfection of 3.8–9.8% would be needed to reproduce the measured limit. Dynamic strain ageing at 100 °C and solute clustering at 120–140 °C are proposed as its causes. The imperfection falls to 2.6% at 160 °C and stays below 1% at 28 and 180 °C.

3. After paint bake, W-temper deformation gave up to 195.8 HV, against 172.6 HV for warm deformation. Warm deformation kept T6-level hardness up to 160 °C, but at 180 °C the hardness fell 16.4% below T6.

The strain path of the critical feature, rather than a single formability number, should therefore decide between W-temper and warm forming of solution-treated AA7075 sheet.

Declaration of generative AI and AI-assisted technologies in the writing process

During the preparation of this work the authors used Claude (Anthropic) to edit the text for clarity and to prepare the figures from the measured data. After using this tool, the authors reviewed and edited the content as needed and take full responsibility for the content of the published article.

Declaration of competing interest

The authors declare that they have no known competing financial interests or personal relationships that could have appeared to influence the work reported in this paper.

Data availability

Data will be made available on request.

Funding

This work was supported by the National Science and Technology Council (NSTC), Taiwan, under grant NSTC 115-2221-E-027-065-MY2.

Appendix A Fracture heights

Table A.1. Measured and predicted fracture heights, with the error of Eq. (3). Each cell gives H_{EXP}/H_{FE} in mm and, below it, E_H in %.

w (mm)	28 °C	100 °C	120 °C	140 °C	160 °C	180 °C
16	18.99/18.26	12.35/12.18	18.84/18.07	16.98/16.77	16.54/15.95	17.04/16.44
	3.84	1.38	4.09	1.24	3.57	3.52
28	19.60/18.92	13.12/12.67	17.21/16.78	17.31/16.79	16.13/15.48	16.48/15.84
	3.47	3.43	2.50	3.00	4.03	3.88
40	19.55/18.89	13.15/12.55	14.62/14.30	15.78/15.12	17.01/16.39	16.78/16.40
	3.38	4.56	2.19	4.18	3.64	2.26
52	17.02/16.08	13.78/13.27	14.97/14.49	15.64/15.09	16.92/16.50	16.87/16.49
	5.52	3.70	3.21	3.52	2.48	2.25
72	16.94/15.73	15.64/15.05	16.29/16.03	17.15/16.86	19.52/18.86	16.58/16.03
	7.14	3.77	1.60	1.69	3.38	3.32
86	15.72/14.95	16.89/16.31	17.04/16.68	18.21/17.76	19.37/18.97	20.58/20.33
	4.90	3.43	2.11	2.47	2.07	1.21
100	15.38/14.25	15.98/15.60	16.78/15.98	17.68/17.39	19.03/18.51	19.87/19.21
	7.35	2.38	4.77	1.64	2.73	3.32

References

[1] K. Zheng, D. J. Politis, L. Wang, J. Lin, A review on forming techniques for manufacturing lightweight complex-shaped aluminium panel components, International Journal of Lightweight Materials and Manufacture 1 (2) (2018) 55–80. doi:10.1016/j.ijlmm.2018.03.006.

[2] E. Scharifi, V. A. Yardley, U. Weidig, D. Szegda, J. Lin, K. Steinhoff, Hot sheet metal forming strategies for high-strength aluminum alloys: A review—Fundamentals and applications, Advanced Engineering Materials 25 (16) (2023) 2300141. doi:10.1002/adem.202300141.

[3] M. Skwarski, A review of sheet warm forming methods for high-strength 7xxx aluminum alloys, Materials Science-Poland 43 (3) (2025) 64–84. doi:10.2478/msp-2025-0031.

[4] M. Skwarski, A review of W-temper forming methods for high-strength 7xxx aluminum alloy sheet, Materials Science-Poland 43 (4) (2025) 79–106. doi:10.2478/msp-2025-0043.

[5] Y. Choi, J. Lee, S. S. Panicker, H.-K. Jin, S. K. Panda, M.-G. Lee, Mechanical properties, springback, and formability of W-temper and peak aged 7075 aluminum alloy sheets: Experiments and modeling, International Journal of Mechanical Sciences 170 (2020) 105344. doi:10.1016/j.ijmecsci.2019.105344.

[6] J. Lee, H. J. Bong, D. Kim, Y.-S. Lee, Y. Choi, M.-G. Lee, Application of combined W-temper and cold forming technology to high-strength aluminum alloy automotive parts, JOM 71 (12) (2019) 4393–4404. doi:10.1007/s11837-019-03779-z.

[7] I. Ismayil, Y.-L. Yang, U. Marimuthu, W.-L. Chen, L.-Y. Chen, H. Hsiao, Warm forming behaviour, ageing response, and microstructure–formability relationship of AA7075-T6 aluminium alloy, Materials Transactions 67 (7) (2026) 1110–1121. doi:10.2320/matertrans.MT-MA2026017.

[8] K. Zheng, Y. Dong, D. Zheng, J. Lin, T. A. Dean, An experimental investigation on the deformation and post-formed strength of heat-treatable aluminium alloys using different elevated temperature forming processes, Journal of Materials Processing Technology 268 (2019) 87–96. doi:10.1016/j.jmatprotec.2018.11.042.

[9] C. Moon, S. Thuillier, J. Lee, M.-G. Lee, Mechanical properties of solution heat treated Al-Zn-Mg-Cu (7075) alloy under different cooling conditions: Analysis with full field

measurement and finite element modeling, Journal of Alloys and Compounds 856 (2021) 158180. doi:10.1016/j.jallcom.2020.158180.

[10] Y. Choi, J. Ha, M.-G. Lee, Y. P. Korkolis, Effect of plastic anisotropy and Portevin-Le Chatelier bands on hole-expansion in AA7075 sheets in -T6 and -W tempers, Journal of Materials Processing Technology 296 (2021) 117211. doi:10.1016/j.jmatprotec.2021.117211.

[11] H. Wang, Y.-b. Luo, P. Friedman, M.-h. Chen, L. Gao, Warm forming behavior of high strength aluminum alloy AA7075, Transactions of Nonferrous Metals Society of China 22 (1) (2012) 1–7. doi:10.1016/S1003-6326(11)61131-X.

[12] W. Huo, L. Hou, Y. Zhang, J. Zhang, Warm formability and post-forming microstructure/property of high-strength AA 7075-T6 Al alloy, Materials Science and Engineering: A 675 (2016) 44–54. doi:10.1016/j.msea.2016.08.054.

[13] T. A. Ivanoff, J. T. Carter, L. G. Hector, Jr., E. M. Taleff, Retrogression and reaging applied to warm forming of high-strength aluminum alloy AA7075-T6 sheet, Metallurgical and Materials Transactions A 50 (3) (2019) 1545–1561. doi:10.1007/s11661-018-5084-3.

[14] S. Royne, H. Laurent, A. Maillard, Optimum heating time for warm forming of AA7075 aluminum alloy in T6 condition, The International Journal of Advanced Manufacturing Technology 133 (11–12) (2024) 6005–6021. doi:10.1007/s00170-024-14084-8.

[15] W.-p. Zhang, H.-h. Li, Z.-l. Hu, L. Hua, Investigation on the deformation behavior and post-formed microstructure/properties of AA7075-T6 alloy under pre-hardened hot forming process, Materials Science and Engineering: A 792 (2020) 139749. doi:10.1016/j.msea.2020.139749.

[16] W.-L. Chen, R.-S. Lee, Novel aging warm-forming process of Al-Zn-Mg aluminum alloy sheets and influence of precipitate characteristics on warm formability, Metals 14 (8) (2024) 844. doi:10.3390/met14080844.

[17] N. Wang, A. Ilinich, M. Chen, G. Luckey, G. D'Amours, A comparison study on forming limit prediction methods for hot stamping of 7075 aluminum sheet, International Journal of Mechanical Sciences 151 (2019) 444–460. doi:10.1016/j.ijmecsci.2018.12.002.

[18] L. Ying, T. Gao, H. Rong, X. Han, P. Hu, W. Hou, On the thermal forming limit diagram (TFLD) with GTN mesoscopic damage model for AA7075 aluminum alloy: Numerical and

experimental investigation, Journal of Alloys and Compounds 802 (2019) 675–693. doi:10.1016/j.jallcom.2019.05.342.

[19] W.-L. Chen, R.-S. Lee, A microstructure-integrated ductile fracture criterion and FE-based framework for predicting warm formability of AA7075 sheets, Metals 15 (6) (2025) 655. doi:10.3390/met15060655.

[20] R. Hill, On discontinuous plastic states, with special reference to localized necking in thin sheets, Journal of the Mechanics and Physics of Solids 1 (1) (1952) 19–30. doi:10.1016/0022-5096(52)90003-3.

[21] Z. Marciniak, K. Kuczyński, Limit strains in the processes of stretch-forming sheet metal, International Journal of Mechanical Sciences 9 (9) (1967) 609–620. doi:10.1016/0020-7403(67)90066-5.

[22] J. W. Hutchinson, K. W. Neale, Sheet necking—II. Time-independent behavior, in: D. P. Koistinen, N.-M. Wang (Eds.), Mechanics of Sheet Metal Forming: Material Behavior and Deformation Analysis, Plenum Press, New York, 1978, pp. 127–153. doi:10.1007/978-1-4613-2880-3_6.

[23] A. K. Ghosh, The influence of strain hardening and strain-rate sensitivity on sheet metal forming, Journal of Engineering Materials and Technology 99 (3) (1977) 264–274. doi:10.1115/1.3443530.

[24] J. W. Hutchinson, K. W. Neale, Sheet necking—III. Strain-rate effects, in: D. P. Koistinen, N.-M. Wang (Eds.), Mechanics of Sheet Metal Forming: Material Behavior and Deformation Analysis, Plenum Press, New York, 1978, pp. 269–285. doi:10.1007/978-1-4613-2880-3_11.

[25] R. A. Ayres, M. L. Wenner, Strain and strain-rate hardening effects in punch stretching of 5182-0 aluminum at elevated temperatures, Metallurgical Transactions A 10 (1) (1979) 41–46. doi:10.1007/BF02686404.

[26] P. G. McCormick, Theory of flow localisation due to dynamic strain ageing, Acta Metallurgica 36 (12) (1988) 3061–3067. doi:10.1016/0001-6160(88)90043-0.

[27] M. Hörnqvist, B. Karlsson, Temperature and strain rate dependence of the dynamic strain aging effect in an Al–Zn–Mg alloy, Materials Science and Technology 22 (2) (2006) 213–222. doi:10.1179/174328406X74284.

[28] J. Robson, P. Jessner, M. Taylor, Z. Ma, Dynamic precipitation in supersaturated Al–Zn–Mg–Cu alloy during warm stretching, Metallurgical and Materials Transactions A 54 (4) (2023) 1131–1141. doi:10.1007/s11661-023-06962-9.

[29] T. Naka, G. Torikai, R. Hino, F. Yoshida, The effects of temperature and forming speed on the forming limit diagram for type 5083 aluminum–magnesium alloy sheet, Journal of Materials Processing Technology 113 (1–3) (2001) 648–653. doi:10.1016/S0924-0136(01)00650-1.

[30] D. Li, A. K. Ghosh, Biaxial warm forming behavior of aluminum sheet alloys, Journal of Materials Processing Technology 145 (3) (2004) 281–293. doi:10.1016/j.jmatprotec.2003.07.003.

[31] S. P. Keeler, W. A. Backofen, Plastic instability and fracture in sheets stretched over rigid punches, Transactions of the ASM 56 (1963) 25–48.

[32] G. M. Goodwin, Application of strain analysis to sheet metal forming problems in the press shop, SAE Technical Paper 680093, SAE International (1968). doi:10.4271/680093.

[33] International Organization for Standardization, Geneva, ISO 12004-2:2021, Metallic materials — Determination of forming-limit curves for sheet and strip — Part 2: Determination of forming-limit curves in the laboratory (2021).

[34] R.-S. Lee, Q.-C. Hsu, Image-processing system for circular-grid analysis in sheet-metal forming, Experimental Mechanics 34 (2) (1994) 108–115. doi:10.1007/BF02325707.

[35] Q.-C. Hsu, Comparison of different analysis models to measure plastic strains on sheet metal forming parts by digital image processing, International Journal of Machine Tools and Manufacture 43 (5) (2003) 515–521. doi:10.1016/S0890-6955(02)00241-9.

[36] Q.-T. Pham, B.-H. Lee, K.-C. Park, Y.-S. Kim, Influence of the post-necking prediction of hardening law on the theoretical forming limit curve of aluminium sheets, International Journal of Mechanical Sciences 140 (2018) 521–536. doi:10.1016/j.ijmecsci.2018.02.040.

[37] H. W. Swift, Plastic instability under plane stress, Journal of the Mechanics and Physics of Solids 1 (1) (1952) 1–18. doi:10.1016/0022-5096(52)90002-1.

[38] E. Voce, The relationship between stress and strain for homogeneous deformation, Journal of the Institute of Metals 74 (1948) 537–562.

[39] Dassault Systèmes Simulia Corp., Providence, RI, Abaqus 2016 Analysis User's Guide, Section 24.2.2, Damage initiation for ductile metals (2016).

[40] D. Thévenet, M. Mliha-Touati, A. Zeghloul, The effect of precipitation on the Portevin-Le Chatelier effect in an Al–Zn–Mg–Cu alloy, Materials Science and Engineering: A 266 (1–2) (1999) 175–182. doi:10.1016/S0921-5093(99)00029-5.

[41] A. Deschamps, G. Fribourg, Y. Bréchet, J. L. Chemin, C. R. Hutchinson, In situ evaluation of dynamic precipitation during plastic straining of an Al–Zn–Mg–Cu alloy, Acta Materialia 60 (5) (2012) 1905–1916. doi:10.1016/j.actamat.2012.01.002.

[42] C. P. Blankenship, Jr., E. Hornbogen, E. A. Starke, Predicting slip behavior in alloys containing shearable and strong particles, Materials Science and Engineering: A 169 (1–2) (1993) 33–41. doi:10.1016/0921-5093(93)90596-7.

[43] A. Deschamps, F. Livet, Y. Bréchet, Influence of predeformation on ageing in an Al–Zn–Mg alloy—I. Microstructure evolution and mechanical properties, Acta Materialia 47 (1) (1998) 281–292. doi:10.1016/S1359-6454(98)00293-6.